Ram-air kite airfoil and reinforcements optimization for airborne wind energy applications

Thedens, Paul; De Oliveira Andrade, Gael; Schmehl, Roland

DOI
10.1002/we.2313

Publication date
2019

Document Version
Final published version

Published in
Wind Energy

Received: 31 December 2017 | Revised: 14 September 2018 | Accepted: 17 December 2018
DOI: 10.1002/we.2313

WILEY

RESEARCH ARTICLE

Ram-air kite airfoil and reinforcements optimization for airborne wind energy applications

Paul Thedens[1,2,3] | Gael de Oliveira[1] | Roland Schmehl[1]

[1]Faculty of Aerospace Engineering, Delft University of Technology, Delft, The Netherlands
[2]Department of Microsystems Engineering (IMTEK), University of Freiburg, Freiburg, Germany
[3]SkySails Power GmbH, Research & Development, Hamburg, Germany

Correspondence
Paul Thedens, Faculty of Aerospace Engineering Kluyverweg 1, 2629 HS Delft, The Netherlands
Email: p.thedens@tudelft.nl

Present Address
Paul Thedens, SkySails Power GmbH Luisenweg 40, 20537 Hamburg, Germany.
Gael de Oliveira, Institut für Mikrosystemtechnik, Georges-Köhler-Allee 102 79110 Freiburg, Germany.

Funding information
AWESCO. EU H2020 ITN, Grant/Award Number: 642682

Abstract

We present a multidisciplinary design optimization method for the profile and structural reinforcement layout of a ram-air kite rib. The aim is to minimize the structural elastic energy and to maximize the traction power of a ram-air kite used for airborne wind energy generation. Because of the large deformations occurring during flight, a fluid-structure interaction (FSI) routine is included in the optimization, which determines the actual deformed rib geometry and its corresponding aerodynamic characteristics. A qualitative comparison between FSI inclusion and exclusion in the optimization is given. Discrepancies in airfoil profile and structural layout are observed.

KEYWORDS

airborne wind energy, airfoil shape optimization, MDO, ram-air kite, reinforcements

1 | INTRODUCTION

Airborne wind energy (AWE) is an innovative technology that uses tethered flying devices to harvest wind energy. Compared with conventional wind turbines, tethered wings may enable large material savings by limiting the need for supporting structures.[1] Replacing towers by tethers provides access to more predictable winds that blow steadier and stronger at higher altitudes.[2] Several configurations are being investigated by the research community and industry. Electricity can be generated with onboard wind turbines and transmitted to the ground by a conducting tether. Flying fast crosswind maneuvers, the turbines are exposed to high relative flow velocities, leading to a high energy yield. The theoretical yield was originally derived by Loyd,[3] and the concept is pursued by US-based company Makani / X.[4-6] Alternatively, the mechanical traction power of a tethered wing can be used to drive a ground-based generator. Operating the wing in pumping cycles with crosswind operation during tether reel-out and de-powering during reel-in results in a positive net energy per cycle. Several companies and research groups pursue this approach. For a full list of institutions that are currently involved in the research and development of AWE systems, we refer to Diehl et al[7] and Schmehl.[8]

The various technology demonstrators employ rigid, hybrid, or soft wings. Rigid wings are made of carbon or glass fiber composites and are maneuvered with flaps like, for example, the system of Makani / X. Soft wings are made of thin woven fabrics and maneuvered with bridles to deform the wing tips, which introduces an aerodynamic moment. Soft kites of the leading-edge inflated (LEI) type combine a single skin canopy with an inflated tubular beam to define a lift-generating shape.[9] Ram-air kites consist of a double skin canopy inflated with air at stagnation pressure.[10] The stagnation pressure is dependent on the air speed, and with higher air speed, and thus higher aerodynamic loading, the pneumatic structure also becomes more stable. Thus, a ram-air wing is a good example for an adaptive pneumatic structure.

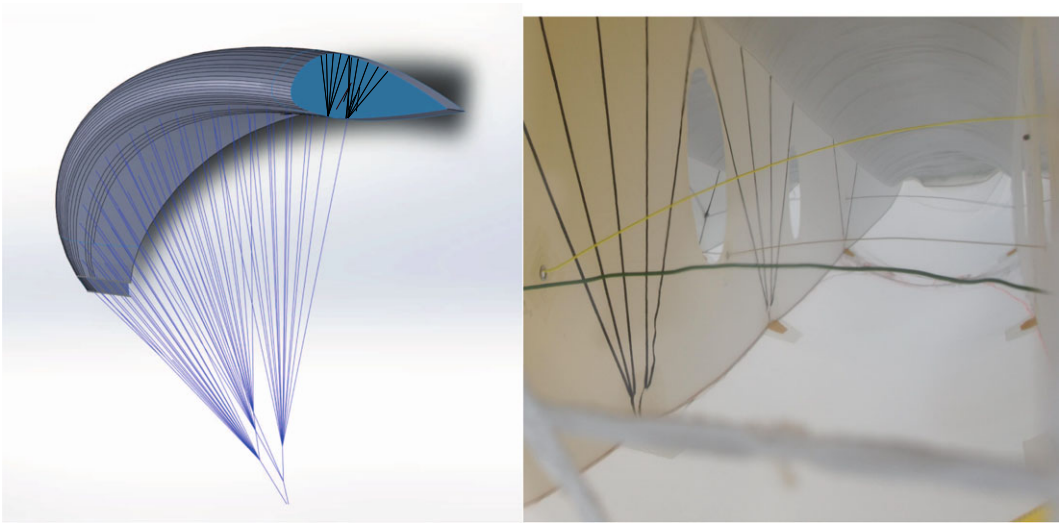

(A) (B)

FIGURE 1 A, Ram-air kite CAD model with indicated rib (blue) and reinforcements (black); B, Structural layout of rib by SkySails. [Colour figure can be viewed at wileyonlinelibrary.com]

Each wing type has distinct advantages for airborne wind energy generation. Rigid wings are durable and can reach higher aerodynamic lift over drag ratios than soft kites because of high aspect ratio wings and very efficient glider profiles, which do not deform during flight. Contrarily, soft kites usually have lower glide ratios (ratio of lift and drag forces) because of their deformable wing profile and lower aspect ratio. Also, the bridle system introduces a considerable amount of aerodynamic drag. Nevertheless, soft kites compensate their lower glide ratio with a large area-to-weight ratio and enables the use of large surface areas. For AWE applications, the tether plays an important role in system scaling and dominates aerodynamic drag.[11] For that reason, soft kites with large wing surface have a similar overall performance compared with high glide ratio rigid wings.

Soft kites are difficult to simulate because the inherent flexibility of the structure leads to large deformations. In turn, the large deflections affect the external flow field and thus also the aerodynamic loading. This strong coupling between structure and air flow generally governs the aerodynamic characteristics of the wing. The main challenge is the drastic increase in model complexity when accounting for fluid-structure interaction (FSI), which however is crucial in many situations for obtaining reliable results for performance measures and structural integrity.

FSI analysis of soft kites and parachutes became feasible with the growth in computational power and the development of numerical tools that tackle the coupling between fluid and structure. Early approaches focused mostly on two-dimensional fluid modeling[12] or resorted to simple three-dimensional approaches to approximate dynamic behavior and glide ratio with panel methods.[13,14] High-fidelity three-dimensional dynamic simulations[15] with several millions of fluid cells started in early 2000, and most recently, the influence of fabric porosity on the aerodynamics was studied.[16]

Aerodynamic loads acting on ram-air kites cause load concentrations especially at the first quarter chord.[17] Reinforcements are introduced to prevent excessive stress at highly loaded parts of the kite. Because of the low pressure acting on the top side of the canopy, the load path goes through the rib to the line attachments points (LAP), which makes the rib a highly loaded structural component in a ram-air kite. Figure 1 illustrates a ram-air kite CAD model with reinforcements (black) attached to a local rib. The reinforcements made of thicker fabric start at the line attachment point and spread out toward the top of the canopy. On the right-hand side, a photograph taken inside an inflated kite from SkySails[18] with the camera view toward the trailing edge can be found. The reinforcement layout has a strong influence on the wing profile during flight and on the lifetime expectancy of the fabric.

The paper presents a multidisciplinary design optimization (MDO) to assess the influence of fabric orientation, reinforcement layout, and airfoil shape on flight performance and rib deformation. A two-dimensional simplified and approximate model is developed to avoid the extensive computations that would be required for high-fidelity soft-kite simulations. The model considers a single rib loaded with a two-dimensional aerodynamic pressure field obtained by integrating the span-wise pressure field. Aerodynamic effects due to the inlets at the leading edge and fabric porosity are neglected, as well as cross-ports (holes in the rib to ensure equal pressure in each cell) in the rib. Viscous effects, surface roughness, and fundamental FSI phenomena are considered. The paper is organized in the following fashion. Section 2 describes the structural, aerodynamic, and FSI model approaches. Section 3 shows the optimization goals for the MDO, and in Section 4, the optimization results and a qualitative comparison of the results with and without FSI can be found. Finally, the conclusion is presented in Section 5.

2 | ANALYSIS OF RAM-AIR KITES

2.1 | Structural model

The deformation of the loaded two-dimensional kite rib is modeled with the finite element (FE) method. To account for large displacements, the analysis is done using the Green-Lagrange strain tensor, leading to a geometrically nonlinear FE formulation. Ram-air kites are often made of

ripstop material, which is a coated woven fabric with coarser warp and filling yarns at intervals so that tears will not spread. The modeling of woven fabric is difficult because of its nonlinear stress-strain behavior and the load ratio dependence, which has a significant influence on the elastic constants.[19] In this paper, the orthotropic Saint Venant-Kirchhoff material model[20] is used, which is valid for small strains. Table 1 shows the chosen material properties for the rib and bridles. The fabric material stiffness is normalized by the fabric's thickness, which is difficult to measure accurately, and therefore given in kN/m. The coated parachute nylon ripstop fabric is taken from a NASA test sheet.[21] For simplification, we assume the same stiffness and Poisson's ratios in warp and weft direction and a shear stiffness of 10% of the Youngs's modulus. The bridle and reinforcements are assumed to be made of Dyneema.[22]

The rib is modeled using constant strain finite elements, whereas the bridles and reinforcements consist of bar elements. In order to obtain a correct load path through the rib, the bridle point (pilot position) is fixed in all degrees of freedom. Additionally, the rearmost LAP is constrained in the chord-wise direction to avoid ill conditioning of the FE system. Since the bridle point is moved to the neutral line for trimming in each iteration, the LAP constraint has a minor effect on the overall deformations (see Section 3.2).

To describe the structural response to pressure loads, the weak form of the FE model as the balance between internal and external force vectors $\mathbf{f}_{int}$ and $\mathbf{f}_{ext}$ is given as

$$\mathbf{R} = \mathbf{f}_{int} - \mathbf{f}_{ext} = \mathbf{K}\mathbf{u} - \mathbf{f}_{ext}. \tag{1}$$

The force vector difference forms the residual **R**, which becomes zero in equilibrium. The internal force vector consists of the stiffness matrix **K** and the displacement vector **u**. The nonlinear equation is solved iteratively with the Newton-Raphson method, where the gradient, ie, tangent stiffness matrix K_T, is given by

$$\mathbf{K}_T = \frac{\partial \mathbf{R}}{\partial \mathbf{u}} = \frac{\partial \mathbf{K}}{\partial \mathbf{u}}\mathbf{u} + \mathbf{K} - \frac{\partial \mathbf{f}_{ext}}{\partial \mathbf{u}}. \tag{2}$$

It should be noted that the external load vector is a deformation-dependent follower load because the pressure acts normal to the body's surface (or edge in the two-dimensional rib) and thus contributes to the tangent stiffness matrix, making it asymmetric.[23] The FE system was implemented as an in-house software and is utilized within the optimization.

2.2 | Aerodynamic model

Flow around airfoils of ram-air kites combines several multiscale phenomena. On the pressure side, bridle attachment points create surface irregularities ("kinks," see Figure 2), over which the flow may separate and eventually reattach. Shape irregularities are softer on the suction side, but dynamic compliance mechanisms can affect boundary layer transition in nonlinear ways.[24] Furthermore, ram-air kites are built of woven fabrics whose surface is neither perfectly impermeable nor hydrodynamically smooth. While direct numerical simulation (DNS) of clean airfoil flows is sometimes feasible,[25] the DNS solution of FSI problems at relatively high Reynolds number remains completely out of reach.[26] This is specially true for conceptual design and optimization purposes.[27,28]

Following current practice in the airfoil design community,[29] we have chosen to solve the flow with a viscous-inviscid interaction (VII) method.[30] Rfoil is a VII code derived from Xfoil:[31] it couples a panel method[32] for the potential flow of the far-field with an integral method (IBL)[33] for the boundary layer flow of the near-field. Flow regions are tightly coupled through the Lighthill interaction law,[34] and the two codes (Rfoil and Xfoil) differ in their handling of turbulent and transitional boundary layers. [35,36]

TABLE 1 Material parameters

Et_{fabric}, kN/m	ν_{12} [-]	E_{bridle}, GPa	d_{bridle}, mm
50	0.3	15	3

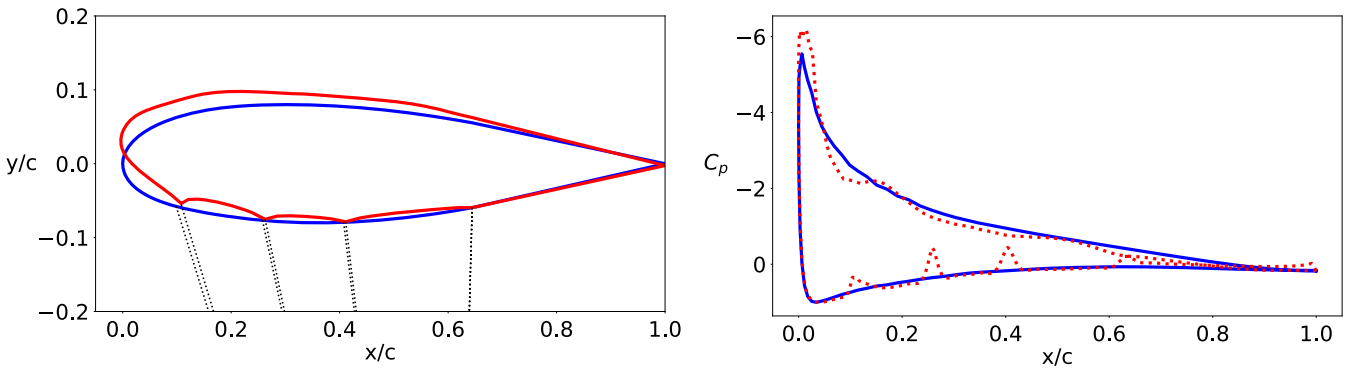

FIGURE 2 Undeformed (blue) and deformed (red) rib profile and its corresponding pressure coefficient distribution. For illustrative purposes, the rib is modeled without reinforcements to emphasize the influence of the kinks on the pressure. During optimization, the reinforcements prevent such large strains to occur [Colour figure can be viewed at wileyonlinelibrary.com]

The turbulent boundary layer formulation of Rfoil was strengthened over the years to perform well in high-Reynolds number cases[35,36] that include local perturbations like those caused by active flow control.[37] In this work, we further enhanced Rfoil's turbulent boundary layer formulation to deal better with the peculiarities of ram-air kite airfoils:

- Separation and reattachment near line attachment points were handled by further improving the numerical implementation details. The main modifications consisted in refining the spatial discretization of kinks, correcting closure relation inconsistencies for low shape factors (H<1.2) that occur upstream of boundary layer kinks, and increasing iteration count.
- Surface roughness of kite fabrics was handled by correcting the turbulent skin-friction correlation according to the recommendations of Betterman[38] through the procedure outlined by Tani.[39]

In terms of work flow, Rfoil receives a geometry and nondimensional flow parameters as inputs and computes pressure distributions or force coefficients for one or more angles of attack. Higher level execution is controlled from Python through a pipe to run Rfoil and the structural solver in batch mode. This approach has proven robust enough for optimization purposes, even when including an FSI routine that requires several Rfoil runs inside an iterative loop.

In Table 2, the flow parameters used for the aerodynamic analysis consisting of apparent wind velocity v_a, air density ρ, and kinematic viscosity ν are shown. The apparent wind velocity is the difference of the wind and kite velocity vectors and can be determined as

$$v_a = \frac{2C_R}{3C_D} v_w, \tag{3}$$

where C_R is the euclidean norm of lift and drag coefficients, and v_w is the wind speed.[1] It should be mentioned that Equation 3 is the maximum apparent wind velocity that can be theoretically achieved in an ideal crosswind operation with optimal reel-out speed. With a variable apparent wind velocity, additional complexity is added to the optimization, which caused convergence issues in the FSI routine. Therefore, we decided to fix the apparent wind speed to 40 m/s, which is obtained with a wind speed of 10 m/s and a glide ratio of 6, often found for ram-air kites.[40] The fixed apparent wind speed can be seen as a design apparent wind speed. In case of more efficient profiles (larger glide ratio) obtained during the optimization, which would result in a higher apparent wind speed, the reel-out speed can be changed such that constant apparent wind speed is realized.

The flow parameters results in a Reynolds number of 11 million. The Reynolds number is kept constant during the optimization even though the chord length is changing its length, but negligible changes in the fluid field due to chord length change were observed.

The bridle drag is an important factor in the power harvesting factor computation because it largely contributes to the total drag. It is assumed that the kite has a total surface area of 40 m^2, a span of 10 m, and consists of 10 cells. Each cell is connected to the main tether with four bridles. The drag contribution from parasitic (C_d), induced, and tether drag[41] is expressed as

$$C_D = C_d + \frac{C_L^2}{\pi e AR} + C_d^{bridle} \frac{10 l_b \cdot d_b + l_t \cdot 2 d_b}{4 A_w}, \tag{4}$$

where e is the Oswald efficiency factor assumed to be 0.6, AR the aspect ratio equal to 2.5, $C_d^{bridle} \approx 1$ the drag coefficient for a cylinder, $l_b = 4$ m the bridle length equal to the chord length, and $l_t = 300$ m being the total tether length.

To obtain a simplified two-dimensional load on the rib, the pressure acting on a single kite cell is integrated over the cell width corresponding to one-tenth of the wing span. The rib in a ram-air kite is loaded because of pressure forces consisting of external aerodynamic and internal ram pressure acting on the canopy. The external pressure is obtained with Rfoil, whereas the internal pressure is assumed to be at stagnation pressure. Combining both internal and external pressure contributions, the pressure coefficients are subtracted ie, the total pressure coefficient is

$$C_p = C_{p_{\text{aero}}} - C_{p_{\text{ram}}}, \tag{5}$$

where $C_{p_{\text{ram}}}$ essentially is 1 because of stagnation pressure. With the assumption of constant internal stagnation pressure, a compression-free load on the rib is guaranteed. It should be noted that the real three-dimensional flow field is not fully represented with a two-dimensional panel solver such as Rfoil. Also, the profile change in between two ribs due to billowing and span-wise arching cannot be presented with this approach.

2.3 | Fluid-structure interaction

The strong coupling between the deforming profile and the air flow is crucial to the analysis. Structural deformations in the rib will induce changes in the pressure field, which will in return induce a new deformation field. This progress is known as FSI and is the central constituent of this optimization. Not only the change in rib shape changes the flow field, but also the elongation of the bridles, which increases the relative angle of attack considered. With every change in design variables, the FSI is run to determine the objective function in a steady and deformed configuration.

TABLE 2 Flow parameters

v_a, m/s	ρ, kg/m^3	ν, m^2/s
40	1.225	1.46×10^{-5}

Dynamics are fully ignored in this approach, thus no mass term is added to the structure. The FSI convergence criterion is measured with the relative error in elastic energy ϵ, and convergence is achieved when the error is below 1×10^{-5}. The relative error in elastic energy is computed as

$$\epsilon = \frac{W_c^n - W_c^{n-1}}{W_c^{n-1}}, \tag{6}$$

with n being the iteration number and W_c the complementary energy expression, derived in Section 3.3. The FSI between Rfoil and the FE simulation is depicted in Figure 3. A pressure distribution determined by Rfoil for the angle of attack, which maximizes the power harvesting factor (PHF), is used to deform the rib structure. In return, the deformed rib profile is fed back to Rfoil to determine a new pressure distribution. The relative error convergence exhibits a clear direction toward force equilibrium between fluid and structure.

The FSI algorithm is described in more detail in Algorithm 1. First, a series of angles of attack is run with Rfoil to find α^*, which maximizes the power harvesting factor. Then, the rib is deformed based on the previously determined pressure field, and the trim position is shifted. This inner loop is run until the relative structural change is below $\epsilon_R < 1 \times 10^{-4}$. With the structure and flow in equilibrium, the new optimal angle of attack α^* is determined for the current rib, and the inner loop is run again. This procedure is repeated until the relative error in complementary energy of 1×10^{-5} for the outer loop is satisfied. The complementary energy was chosen as the FSI convergence metric because it includes both deformations and applied forces, which is a tighter criterion than pure deformations.

During the FSI, Rfoil reacts very sensitively on small changes in the trailing edge deformation, causing oscillations in energy. The remedy is to make the area behind the rearmost bridle rigid. In a three-dimensional structure, the kite's trailing edge is supported by the canopy and arching of the kite, which cannot be reproduced in a two-dimensional approach. The rigid trailing edge approximation is merely a measure to obtain convergence and thereby enable the study of FSIs near the leading edge and mid-section of the rib.

3 | DESIGN OF RAM-AIR KITE AIRFOILS

3.1 | Airfoil shape design space

Airfoil profile optimization has a broad application in aerospace for various design applications, such as finding profiles, which maximize lift or glide ratio. Incorporating the profile into an optimization routine requires a parametrization that is able to describe a variety of profiles for a low number of design parameters. The class shape transform (CST) parametrization is such a method that represents shapes of aerodynamic bodies with a finite set of parameters. The method was originally introduced by Brenda Kulfan from Boeing[42] and has seen extensive use in aerodynamic and multidisciplinary design optimization (MDO) applications. Notable applications to wing design can be found in Ciampa et al,[43] whereas interesting extensions have been proposed by Straathof.[44] A comparison of airfoil parametrization methods is presented by Sirpawadkul et al.[45]

The design space for the rib profile was chosen to be CST airfoil parameters consisting of the product of a class function $C_{(t)} : \mathbb{R} \to \mathbb{R}$ and a shape function $S_{(t,A_i)} : \mathbb{R}^{1+N} \to \mathbb{R}$, where N represents the order of the parametrization, and A_i is a tuple of N shape coefficients. The class function provides the base features of generic airfoil shapes, whereas the shape function tailors the behavior of the class function to represent specific airfoils. The shape of airfoil top (up/suction) and bottom (down/pressure) surfaces is written as

$$\eta(t) = \begin{cases} \eta_{(t)}^{\text{top}} = C_{(t)} S_{\left(t, A_i^{top}\right)}, \\ \eta_{(t)}^{\text{bot}} = -C_{(t)} S_{\left(t, A_i^{bot}\right)}, \end{cases} \tag{7}$$

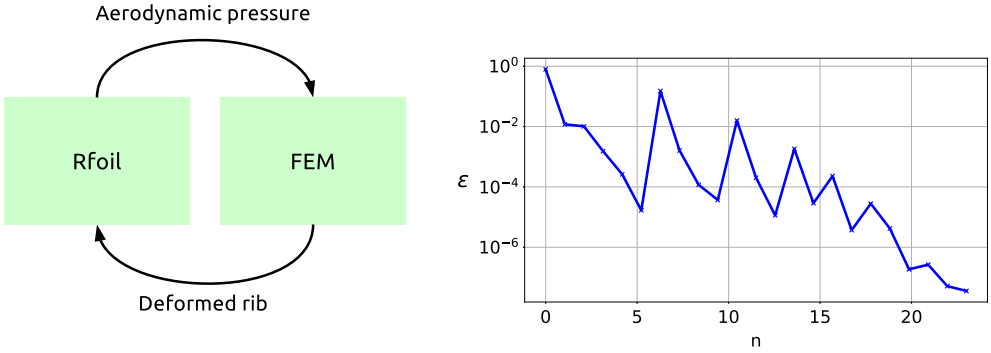

FIGURE 3 Fluid-structure interaction (FSI) schematics and its convergence measured as relative error ϵ against number of iterations [Colour figure can be viewed at wileyonlinelibrary.com]

Algorithm 1 Optimization algorithm with FSI.

```
Initialize design variables x
while NSGA II not converged do
    Initialize FSI (u_t = 0)
    while ϵ > 1e-5 do
        Run Rfoil to obtain lift and drag polar
        Find ζ_max and α* for current configuration
        while ϵ_R > 1e-4 do
            Run FE model with C_p(α*) to obtain u_{t+1}
            Move bridle point to neutral line
        end while
        Update deformed airfoil shape for Rfoil
    end while
    Update design variables x
end while
```

$$\textit{where}\begin{cases} t = x/c \in [0,1] & \text{nondimensional chord-wise coordinate} \\ \eta = z/c & \text{nondimensional thickness coordinate} \\ A_i^{\text{top}} & \text{shape coefficient top side} \\ A_i^{\text{bot}} & \text{shape coefficients bottom side} \\ i = 0, 1, 2 \ldots M & \text{index of shape coefficients} \\ M = N - 1 & \text{degree of parametrization.} \end{cases} \tag{8}$$

The class function for airfoils with rounded leading edges and sharp trailing edges is written as

$$C_{(t)} = (1-t)\sqrt{t}. \tag{9}$$

The shape function is a polynomial of order N (degree $M = N - 1$) obtained by linear combination of the Bernstein polynomial basis with the A_i shape coefficients

$$S_{(t,A_i)} = \sum_{i=0}^{M} A_i s_{(t)}^{iM}. \tag{10}$$

The set of Bernstein polynomial functions of order N (degree $M = N - 1$) forms a complete basis for the space of polynomials of degree $M = N - 1$. A linear homeomorphism exists between the Bernstein and canonical polynomial bases, but the Bernstein basis has more favorable numerical properties for higher order settings with limited floating point precision. The Bernstein basis functions of order N (degree $M = N - 1$) are given in terms of the binomial coefficient

$$s_{(t)}^{iM} = \binom{M}{i} t^i (1-t)^{M-i} \quad \text{with} \quad i = 0, 1, 2 \ldots M. \tag{11}$$

The binomial coefficient is often best visualized in terms of Pascal's triangle, and the above expressions apply to parametrization of arbitrary order. The basis of order N comprises all bases of lower order, which is a favorable property in optimization, because a higher order N includes all possible solutions of the lower orders. CST airfoil parametrization has proven itself as a solid approach to represent a full set of airfoil shapes, which can be used for optimization purposes.

3.2 | Aerodynamic goals

Kites for AWE applications produce maximum power output with a specific wing configuration that maximizes the pulling force due to lift and drag. The theoretical power extraction was initially derived in the paper by Loyd,[3] where the power output from kites in drag and lift mode were studied. The maximum power harvesting factor $\zeta_{\max}$ is expressed as the ratio between harvested power and available power equating to

$$\zeta_{\max} = \frac{4}{27} C_R (1 + E^2), \tag{12}$$

with C_R being the Euclidean norm of the lift and drag coefficients C_L and C_D, and E is the glide ratio. The power harvesting factor is chosen as the performance metric in the optimization and is to be maximized for a deformed profile. Unlike rigid aircraft, which can be constantly trimmed by changing the elevator angle on the horizontal stabilizer, soft kites have a fixed trim. The trimming is done by positioning the bridle point, ie, the position where all bridles connect below the canopy, along the neutral line where the all moments are in equilibrium. Since the kite deforms

during operation, this neutral line is not known a priori and usually found experimentally. To ensure moment equilibrium at all stages during the optimization, the kite is trimmed in each FSI iteration by moving the bridle point along the chord to the neutral line while keeping the bridle length constant in *y*-direction. To ensure that the reaction force at the fourth LAP is not compromising the deformation, several rib configurations were manually tested, and it was found that the reaction force is approximately 1×10^6 times smaller than the reaction force at the bridle point. The optimal angle of attack α^* in each FSI iteration, which maximizes $\zeta_{\max}$, is found with

$$\alpha^* = \arg\max_{\alpha} \frac{4}{27} C_R(\alpha)(1 + E^2(\alpha)). \tag{13}$$

3.3 | Structural goals

The reinforcements are modeled as bar elements starting at each of the four LAPs in a group of five. For each group of reinforcements, two independent angles are defined to reduce the number of total design variables to eight for the reinforcements only, shown in Figure 4A. By changing the absolute orientation angle ϕ_i, the whole group of reinforcements at LAP *i* is rotated, whereas changing the relative orientation angle γ_i changes the spread of reinforcement group *i*, respectively. The orthotropic material angle θ is defined as the angle between the *x*-axis and the warp threading of the fabric.

Only straight bar reinforcements are considered oriented like rays starting from the four LAPs. The bars are embedded in the rib continuum mesh and add stiffness to all elements, which the bars are crossing.[46] As shown in Figure 4B, the nodes **i** and **j** cross the CST element at two edges, contributing to nodes **1**, **2**, and **3** as a weighted average rather than introducing new nodes. The advantage of this approach is that the rib mesh does not require refinement at areas where several reinforcements are converging. Also, no remeshing of the structure is required, and the sparsity pattern of the stiffness matrix is therefore unchanged, which speeds up the computation.

Compliance minimization is a common metric for structural optimization and effectively maximizes the structural stiffness. For geometrically nonlinear structures, the compliance expression does not fully describe the force-displacement relationship because of its nonlinearity. Instead, the complementary energy expression is chosen as a metric to describe the overall structural stiffness.[47] The complementary energy is computed as the integral of the deformation vector **u** with respect to the external load vector **f**. [48] This expression can be rewritten as

$$W_c = \int_0^{\mathbf{f}^*} \mathbf{u}\, d\mathbf{f} = \mathbf{u}^{*^T}\mathbf{f}^* - U^*(\mathbf{u}), \tag{14}$$

where the asterisk denotes the quantities in equilibrium state, and *U* is the strain energy.

3.4 | Material weave direction

Before proceeding to the full multiobjective design optimization, the design space of the two objectives is explored, as shown in Figure 5. It depicts both objectives normalized with their initial value at $\theta = 0$ as a function of the material orientation angle θ only, including (red) and ignoring (blue) the FSI routine, respectively. The chosen airfoil shape is equivalent to the initial design for the optimization introduced in the next section.

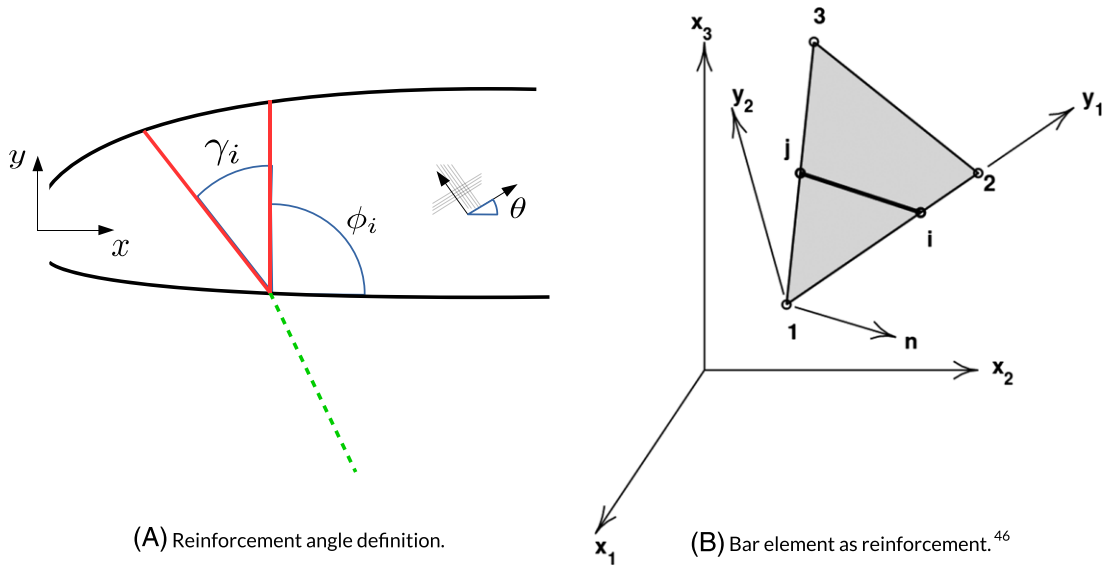

(A) Reinforcement angle definition. (B) Bar element as reinforcement. [46]

FIGURE 4 Reinforcement modeling [Colour figure can be viewed at wileyonlinelibrary.com]

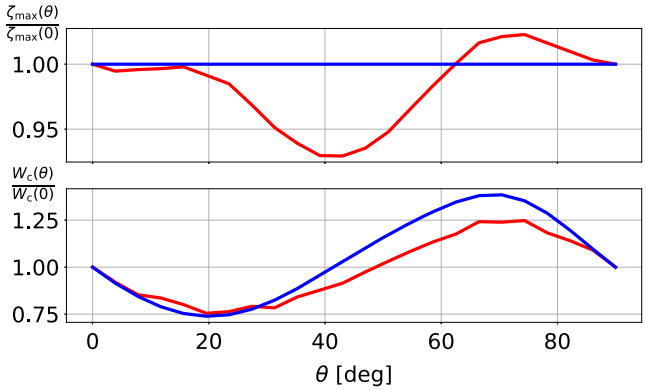

FIGURE 5 Material orientation angle θ against normalized power harvesting factor and complementary energy in deformed (red) and undeformed (blue) states [Colour figure can be viewed at wileyonlinelibrary.com]

By excluding the FSI routine, the pressure load is applied to the undeformed profile only, and from it the complementary energy is determined. As a result, a change in material orientation has no influence on the power harvesting factor, and an overall variation of approximately 60% in complementary energy is observed. The lowest complementary energy is found at 20°, which corresponds to the overall stiffest structural layout in the given design space. The highest value, on the other hand, corresponds to the material orientation such that the rib is mostly loaded in shear, causing maximum deformation.

Including the FSI routine introduces a dependence of the material orientation on the PHF, which peaks at 70°, causing the structure to deform in an aerodynamically economical manner. Conversely, at approximately 45° material orientation angle, the deformed rib bulges at the suction side, reducing the effective PHF. For the complementary energy, a flat plateau can be seen between 10° and 30° and a peak at 70°. For the initial airfoil, both objectives clearly work against each other, as their individual optima lay at different locations. Also, the peak in PHF results in a maximum in complementary energy, which means that the profile deforms in such a way that the PHF is higher compared with the initial geometry. This peculiar phenomenon was not generally observed, but rather a coincidence for this particular airfoil.

4 | EFFICIENT DESIGNS ARE MULTIDISPLINARY COMPROMISES

4.1 | Multiobjective optimization

As depicted in the previous section, both optimization objectives do not comply with each other. This is a common problem in multidisciplinary design optimization and can only be solved by compromising between the two objectives. The Pareto frontier illustrates the boundary between feasible and infeasible solution space of two objectives and is obtained through the optimization routine. We follow the MDO with the NSGAII (Non-dominated Sorting Genetic Algorithm-II), which is a genetic, derivative-free method for numerical optimization of nonconvex continuous optimization problems.[49] The power harvesting factor, and especially the complementary energy expression, vary in a highly nonlinear way, with small changes in the design vector due to the FSI analysis. NSGAII is capable of handling strong nonlinearities, *NaN* value exceptions, and nonconvexity, and is therefore chosen as optimizer. Also, NSGAII allows computing an entire Pareto front because the optimizer creates sets of solution generations, which approach the infeasible boundary where the Pareto frontier resides.

The objective function of the MDO consists of the power harvesting factor ζ_{max} and the complementary energy W_c. The design variable vector consists of $\mathbf{x} = \left[\theta, \phi_i, \gamma_i, w_j^{top}, w_j^{bot}\right]^T$, with the fiber angle, the absolute and relative reinforcements orientation angles, and the CST weights for the top and bottom side of the airfoil, respectively. The optimization problem is stated as

$$
\begin{aligned}
\underset{\mathbf{x}}{\text{minimize}} \quad & f(\mathbf{x}) = (W_c(\mathbf{x}), -\zeta_{max}(\mathbf{x})) \\
\text{subject to} \quad & \theta_i^{min} \le \theta \le \theta_i^{max} \\
& \phi_i^{min} \le \phi_i \le \phi_i^{max}, \quad i = 1, \dots, K \\
& \gamma_i^{min} \le \gamma_i \le \gamma_i^{max}, \quad i = 1, \dots, K \\
& w_j^{top,\,min} \le w_j^{top} \le w_j^{top,\,max}, \quad j = 1, \dots, N \\
& w_j^{bot,\,min} \le w_j^{bot} \le w_j^{bot,\,max}, \quad j = 1, \dots, N,
\end{aligned}
$$

where K is the number of reinforced LAPs, and N is the Bernstein polynomial function order. The PHF ζ_{max} is defined negatively to comply with a minimization statement. The bounds on the optimization variables can be found in Table 3. In this paper, the order of Bernstein polynomial function is chosen to be six, and their bounds are based on a collection of airfoil data, including thick and high lift airfoil designs.

TABLE 3 Box constraints and initial condition

variable	θ [deg]	ϕ [deg]	γ [deg]	w_1^{top}	w_2^{top}	w_3^{top}	w_4^{top}	w_5^{top}	w_6^{top}
Initial	45	90	15	0.3	0.3	0.3	0.3	0.3	0.3
Min	0	45	5	0.0874	0.1028	0.0267	-0.0444	-0.0413	-0.1429
Max	90	135	20	0.5254	0.5438	0.7101	0.6479	0.4681	0.5438
				w_1^{bot}	w_2^{bot}	w_3^{bot}	w_4^{bot}	w_5^{bot}	w_6^{bot}
Initial				0.3	0.3	0.3	0.3	0.3	0.3
Min				0.0553	-0.1324	-0.2729	-0.2852	-0.3228	-0.4128
Max				0.6446	0.7203	0.9058	0.7813	0.3194	0.4164

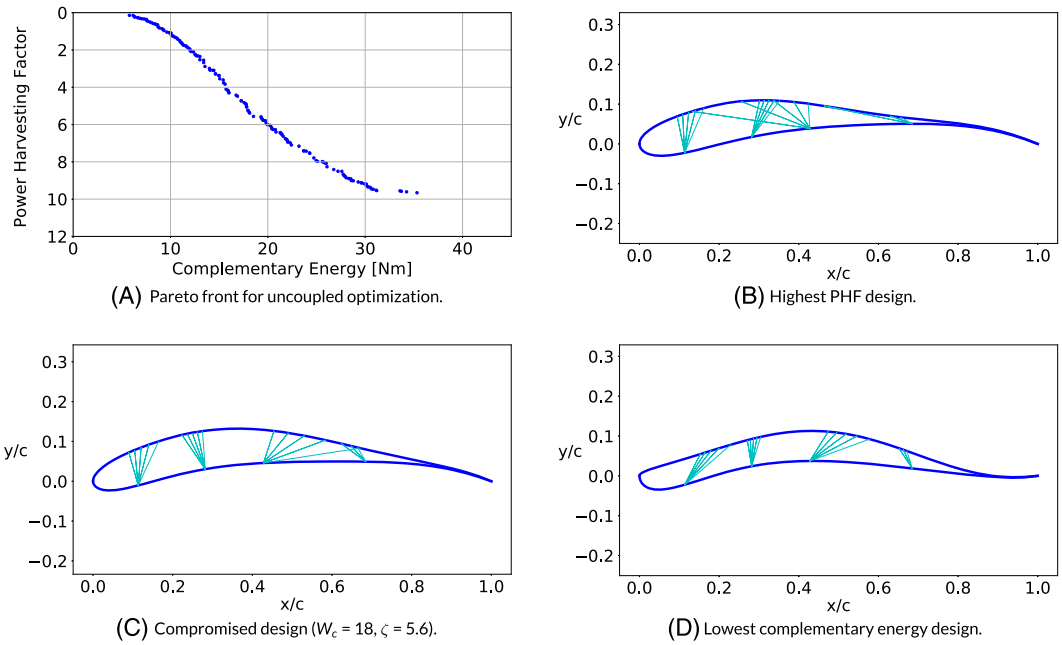

(A) Pareto front for uncoupled optimization. (B) Highest PHF design. (C) Compromised design (W_c = 18, ζ = 5.6). (D) Lowest complementary energy design.

FIGURE 6 Pareto front and ribs for uncoupled case [Colour figure can be viewed at wileyonlinelibrary.com]

4.2 | Optimization of undeformed structure

The NSGAII is run with the full set of 21 design parameters for the uncoupled and FSI cases. Figure 6A shows the resulting Pareto front between the two objectives ζ_{max} and W_c for uncoupled optimization. All solutions left of the frontier are infeasible, because a higher ζ_{max} cannot be achieved without an increase in W_c. Similarly, all solutions right of the frontier are feasible but not optimal, because a more dominant solution along the frontier exists. Hence, a Pareto front gives the user an idea how to make optimal tradeoffs between two objectives.

Figure 6B-D depict three distinct airfoil shapes and reinforcement layouts found on the Pareto front. Figure 6B is the profile with the highest obtained PHF of all individuals. The profile has a maximum thickness of approximately 10% and a thin trailing edge. Choosing a high-PHF design on the Pareto front, the resulting airfoil shape is a sharp profile. The reinforcements are oriented toward the suction side, where the first two sets are more compressed in a direction, whereas the reinforcements from the third LAP spread out.

Conversely, the resulting rib for lowest complementary energy design in Figure 6D is shaped such that the resulting complementary energy is minimized. This is done by essentially forming the aerodynamically worst performing profile such that the pressure forces acting on the rib are minimum. The reinforcements are oriented toward the mid-chord location, and the fiber orientation angle is 10°.

The rib with a compromised design in Figure 6C still exhibits a sharp profile with more camber compared with the high-PHF design. The reinforcement orientation spreads toward the first third of the chord.

4.3 | Optimization of deformed structure with FSI

The Pareto front including the FSI in Figure 7A exhibits a larger nonfeasible region compared with the uncoupled front. The maximum PHF of the uncoupled solution is almost twofold of the FSI case. Also, the complementary energy is higher for the same PHF in case of the FSI frontier, which is caused by a larger rib deformation.

For the optimal solution of the highest PHF design in Figure 7B, the profile shows clear differences to the uncoupled design. A larger nose radius and overall thicker airfoil are given by the optimizer when the maximization of the PHF is considered only. The reinforcement orientation

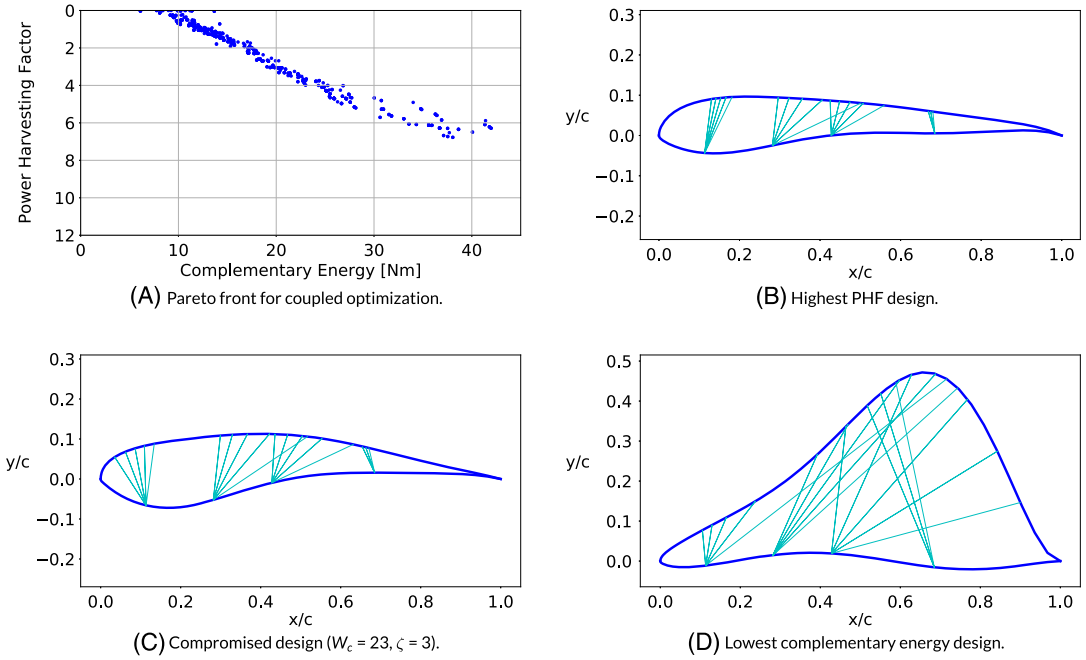

FIGURE 7 Pareto front and ribs for fluid-structure interaction (FSI) case [Colour figure can be viewed at wileyonlinelibrary.com]

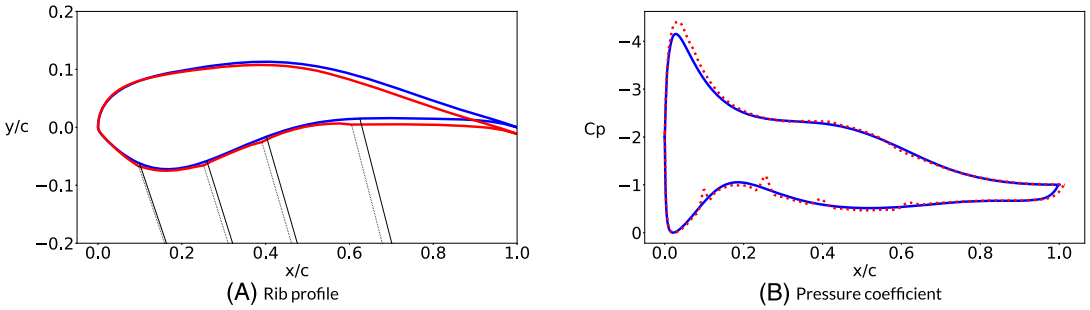

FIGURE 8 Deformed (red) and undeformed (blue) compromised rib design [Colour figure can be viewed at wileyonlinelibrary.com]

is characterized by spreading over the top surface in combination with a material orientation angle of 7°. The optimal solution of the lowest W_c design in Figure 7D is a wedge-like profile with a maximum thickness at 70% chord. Again, an aerodynamically poor design is found, which drastically reduces the overall pressure load and therefore minimizes the complementary energy. Also, the optimal compromised optimum in Figure 7C is a thicker airfoil with larger nose radius compared with the uncoupled optimum.

A qualitative inspection on the compromised designs leads to more insight of imperative design choices when the FSI is included in the design optimization of ram-air kite ribs. Figure 8 outlines the undeformed and deformed rib and resulting pressure distribution in its final shape after FSI convergence. Critical aspects are the change in curvature on the top side, the small kinks at the bottom side at each LAP, and the structural arching between the last two LAPs. Nonoptimal designs typically show a deformed leading edge nose, which is pulled toward the pressure peak, and the final shape differs from the nose shape initially intended to design. In case of the optimum designs found on the Pareto front, the nose is slightly thicker and mainly resists the traction due to the combined structural layout of profile shape as well as material and reinforcement orientation.

Elongation occurs mainly on the top side of the rib, where most aerodynamic forces act. The result is twofold—a nonsmooth top side causes turbulent flow phenomena, which generally reduce lift, whereas arching increases the local camber line, and as can be seen in the pressure coefficient, causes a decrease in pressure, ie, increase in lift. It should be noted that Rfoil fails to fully present the physical phenomena of detached turbulent flow, and as a result, overestimates the produced lift force. Therefore, the pressure distribution should be interpreted with care, and the local pressure reduction due to increased camber may not be as prominent. Nevertheless, an imperative design choice is the correct placement of the reinforcements to locally reduce kinks and shape the bulging in a economical manner such that the flow stays attached. All these effects would not be taken into account when considering the uncoupled case only.

Another aspect that becomes apparent using FSI is the trim and optimal angle of attack, which change between 10% and 30% compared with the uncoupled case, depending on the chosen design optimum on the Pareto frontier. In general, the deformed rib and extended bridles increase the relative angle of attack, and therefore the trim position. Uncoupled approaches are not able to represent this effect, and the reinforcement layout may not lay on the main load path.

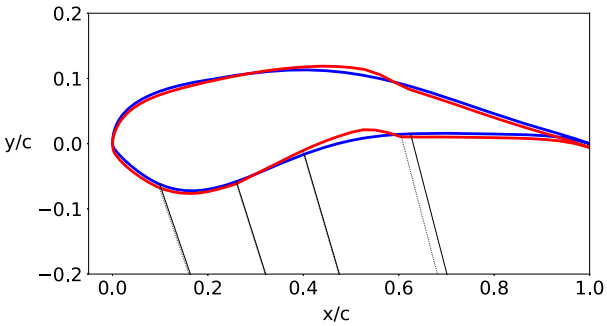

FIGURE 9 Undeformed (blue) and deformed (red) rib geometry with wrinkling model employed [Colour figure can be viewed at wileyonlinelibrary.com]

Finally, the PHF with the FSI for the compromised profile is approximately 35% lower than for the uncoupled solution. This has to be taken into account for system design and scaling. Utilizing the FSI in the optimization routine gives a more conservative result and the best design choice for the rib in deformed flight state.

4.4 | Wrinkling

Wrinkling is a local buckling phenomenon that occurs in thin sheet metals and fabrics when the structure is predominantly loaded in uni-direction, and as a result the smaller principal stress component anywhere in the structure becomes negative. In a wrinkled state, the fabric deforms out of plane, and the in-plane fabric contraction depends on the load and material properties. The out of plane deformation of the wrinkles can be modeled with thin shell elements, but in many applications, the actual wrinkle shape is of less interest. Instead, a wrinkling model that models the average out-of-plane deformation in a finite element can be employed, and the stress state indicates the wrinkle direction.

Some rib layouts during the optimization exhibit compressive stress at the bottom side between the LAP. This compression occurs because generally, the load on top of the wing profile is larger than on the bottom side. Without employing a wrinkling model, the compressive strength of the rib is overestimated. We therefore incorporated a wrinkling model[50] based on the tension field theory[51] to measure the difference in rib deformations and therefore PHF and complementary energy. Running the optimization with the wrinkling model was unsuccessful because of the sensitive numerical behavior of the model, ie, mesh quality and load magnitude have a drastic influence on the convergence behavior.

Figure 9 shows the compromised design layout and its deformation determined with the wrinkling model. A clear distinction in deformation between the third and fourth LAP can be seen. This deformation originates from the reduced stiffness due to compression and results in a more dominant bulging. The PHF for the deformed rib is 43% lower than computed without the wrinkling model. The complementary energy change is only 13%, even though the deformations suggest otherwise. The reason for such a small energy change is due to wrinkling, which does not increase elastic strain energy.

5 | CONCLUSIONS

The paper describes a multidisciplinary design optimization for a ram-air kite in its deformed and trimmed state. The aim is to find an optimum wing profile as well as material orientation and reinforcement layout that maximize the power harvesting factor and at the same time reduce structural deformations. The optimization utilizes an FSI routine, which is run until both fluid flow and structural deformation are in equilibrium. A qualitative description of the FSI algorithm is given, and its convergence is shown.

The main conclusion drawn from the study is the significant influence FSI has on the optimal design and that an optimal design determined with the developed method might even perform worse in undeformed state but can be superior during operation. It therefore becomes evident that including the rib deformation is paramount if an optimum is to be found, which represents an operating kite. Regarding numerical profile optimizations for ram-air kites, this methodology is a first approach and, to the best knowledge of the authors, has not been considered before.

With our FSI approach, no dynamic effects are taken into account, and the algorithm is run until a static equilibrium state is found. This required a rigid trailing edge and a support in x-direction at the rear LAP. These restrictions potentially have a direct influence on the optimization results, but are not necessary if a three-dimensional kite geometry is employed. Therefore, future studies should account for the whole three-dimensional kite geometry to obtain a more reliable deformed shape and the resulting flow field. Reduction to a two-dimensional model leaves important structural phenomena, such as arching of the canopy and side forces due to the kite's span-wise curvature out. As mentioned in Section 4.4, certain stress states in thin fabrics cause the material to wrinkle, which cause in-plane contraction. The deformations of the fabric under the wrinkling state might be very different than one determines without using a wrinkling model. Next to the above mentioned sources of errors due to simplifications, the wrinkling model is crucial for a more realistic kite model and should be employed in future optimization runs.

Finally, lift and drag forces from a three-dimensional finite-wing analysis should be employed to avoid errors in deformations and power harvesting factor.

ACKNOWLEDGEMENTS

Paul Thedens and Roland Schmehl are supported financially by the project AWESCO (H2020-ITN-642682), funded by the European Union's Horizon 2020 research and innovation programme under the Marie Sklodowska-Curie grant agreement No. 642682. The authors have declared no conflict of interest, and also would like to thank Bernd Specht and Manfred Quack from SkySails Power GmbH for providing illustrations and feedback.

ORCID

Paul Thedens https://orcid.org/0000-0003-4545-2361
Gael de Oliveira https://orcid.org/0000-0003-0545-7299
Roland Schmehl https://orcid.org/0000-0002-4112-841X

REFERENCES

1. Ahrens U, Diehl M, Schmehl R, eds. *Airborne Wind Energy*, Green Energy and Technology. Berlin Heidelberg: Springer; 2013. https://doi.org/10.1007/978-3-642-39965-7
2. Archer CL, Caldeira K. Global assessment of high-altitude wind power. *Energies*. 2009;2(2):307-319. https://doi.org/10.3390/en20200307
3. Loyd ML. Crosswind kite power. *J Energy*. 1980;4(3):106-111. https://doi.org/10.2514/3.48021
4. Makani / X. https://x.company/makani/. Accessed June 7, 2018.
5. Makani / X. Makani's first commercial-scale energy kite. https://www.youtube.com/watch?v=An8vtD1FDqs. Accessed 7 June 2018.
6. Fuller L. Ride like the wind: Makani energy kite test flights in the works, lift off later this year. West Hawaii Today, 27 August 2018 edition. http://www.westhawaiitoday.com/2018/08/27/north-hawaii-news/ride-like-the-wind-makani-energy-kite-test-flights-in-the-works-lift-off-later-this-year/. Accessed September 3, 2018.
7. Diehl M, Leuthold R, Schmehl R, eds. *The International Airborne Wind Energy Conference 2017: Book of Abstracts*. Freiburg, Germany: University of Freiburg | Delft University of Technology; 2017. https://doi.org/10.6094/UNIFR/12994
8. Schmehl R, ed. *Airborne Wind Energy – Advances in Technology Development and Research*, Green Energy and Technology. Singapore: Springer; 2018. https://doi.org/10.1007/978-981-10-1947-0
9. Oehler J, Schmehl R. Aerodynamic characterization of a soft kite by in situ flow measurement. *Wind Energy Sci*. 2019;4(1):1-21. https://doi.org/10.5194/wes-4-1-2019
10. Dunker Storm. Ram-air wing design considerations for airborne wind energy. In: Ahrens U, Diehl M, Schmehl R, eds. *Airborne Wind Energy*, Green Energy and Technology. Berlin Heidelberg: Springer; 2013:517-546. https://doi.org/10.1007/978-3-642-39965-7_31
11. Argatov I, Silvennoinen R. Efficiency of traction power conversion based on crosswind motion. In: Ahrens U, Diehl M, Schmehl R, eds. *Airborne Wind Energy*, Green Energy and Technology. Berlin Heidelberg: Springer; 2013:65-79. https://doi.org/10.1007/978-3-642-39965-7_4
12. Mittal S, Saxena P, Singh A. Computation of two-dimensional flows past ram-air parachutes. *Int J Numer Methods Fluids*. 2001;35(6):643-667. https://doi.org/10.1002/1097-0363(20010330)35:6<643::aid-fld107>3.0.co;2-m
13. Chatzikonstantinou T. Recent advances in the numerical analysis of ram air wings—the three dimensional simulation code PARA3D. In: Proceedings of the Aerospace Design Conference; 1993; Irvine,CA, USA:1203. https://doi.org/10.2514/6.1993-1203
14. Altmann H. Numerical simulation of parafoil aerodynamics and dynamic behavior. In: Proceedings of the 20th AIAA Aerodynamic Decelerator Systems Technology Conference and Seminar; 2009; Seattle, WA:2947. https://doi.org/10.2514/6.2009-2947
15. Stein K, Benney R, Kalro V, Tezduyar TE, Leonard J, Accorsi M. Parachute fluid-structure interactions: 3-D computation. *Comput Methods Appl Mech Engng*. 2000;190(3-4):373-386. https://doi.org/10.1016/s0045-7825(00)00208-5
16. Takizawa K, Tezduyar TE, Terahara T. Ram-air parachute structural and fluid mechanics computations with the space-time isogeometric analysis (ST-IGA). *Comput Fluids*. 2016;141:191-200. https://doi.org/10.1016/j.compfluid.2016.05.027
17. Air Turquoise SA. Nucleon 25 – force measurement on each riser. *Test Report*, Villeneuve, Switzerland; 2009. http://www.para-test.com/images/Test_Report/PPG_measure/2009/2009-09-29_nucleon25_ppg.pdf
18. SkySails Marine. https://www.skysails.info/en/skysails-marine/skysails-propulsion-for-cargo-ships/references/. Accessed June 8, 2018.
19. Uhlemann J, Stranghöner N, Saxe K. Stiffness parameters for architectural fabrics: an analysis of two determination procedures. *Struct Eng Int*. 2015;25(1):9-19. https://doi.org/10.2749/101686614X14043795570291
20. Ogden RW. *Non-Linear Elastic Deformations*. New York: Courier Corporation, Dover Publications; 1997.
21. Lin JK, Shook LS, Ware JS, Welch JV. Flexible material systems testing. NASA/CR-2010-216854, Hampton, VA, USA, NASA Langley Research Center; 2010. http://hdl.handle.net/2060/20100038749
22. Marlowropes, Dyneema D12 SK99 data sheet. https://marlowropes.com/system/files_force/downloads/D12\ignorespaces020216.pdf. Accessed June 7, 2018.
23. Wriggers P. *Nonlinear Finite Element Methods*. Berlin Heidelberg: Springer Verlag; 2008. https://doi.org/10.1007/978-3-540-71001-1
24. Carpenter PW, Morris PJ. The effect of anisotropic wall compliance on boundary-layer stability and transition. *J Fluid Mech*. 1990;218:171-223. https://doi.org/10.1017/S0022112090000970

25. Vinuesa R, Hosseini SM, Hanifi A, Henningson DS, Schlatter S. Pressure-gradient turbulent boundary layers developing around a wing section. *Flow, Turbul Combust*. 2017;99(3-4):613-641. https://doi.org/10.1007/s10494-017-9840-z
26. Slotnick J, Khodadoust A, Alonso J, Darmofal D, Gropp W, Lurie E, Mavriplis D. CFD Vision 2030: A path to revolutionary computational aerosciences. NASA/CR-2014-218178, Hampton, VA, USA, Langley Research Center; 2014. http://hdl.handle.net/2060/20140003093
27. Sørensen NN, Mendez B, Munoz A, Sieros G, Jost E, Lutz T, Papadakis G, Voutsinas S, Barakos GN, Colonia S, other. CFD code comparison for 2d airfoil flows. *J Phys: Conf Ser*. 2016;753:082019. https://doi.org/10.1088/1742-6596/753/8/082019
28. Yilmaz ÖC, Pires O, Munduate X, et al. Summary of the blind test campaign to predict the high Reynolds number performance of DU00-W-210 airfoil. In: Proceedings of 35th Wind Energy Symposium., 2017-0915, American Institute of Aeronautics and Astronautics, 35th Wind Energy Symposium, Grapevine, TX, United States, 09/01/2017. https://doi.org/10.2514/6.2017-0915
29. Timmer WA, Bak C. Aerodynamics characteristics of wind turbine blade airfoils. In: Brøndsted P, Nissen RPL, eds. *Advances in Wind Turbine Blade Design and Materials*, Woodhead Publishing Series in Energy: Woodhead Publishing; 2013:109-149.
30. Veldman AEP. Boundary layers in fluids, Lecture Notes in Applied Mathematics, University of Groningen; 2008. http://www.math.rug.nl/~veldman/Colleges/grenslaag/Oud/BoundaryLayers2008.pdf
31. Drela M. Xfoil: An analysis and design system for low Reynolds number airfoils. In: Mueller TJ, ed. *Low Reynolds Number Aerodynamics*, Lecture Notes in Engineering, vol. 54. Berlin-Heidelberg: Springer; 1989:1-12. https://doi.org/10.1007/978-3-642-84010-4_1
32. Katz J, Plotkin A. *Low-Speed Aerodynamics (Cambridge Aerospace Series)*. Cambridge: Cambridge University Press; 2001. https://doi.org/10.1017/CBO9780511810329
33. Schlichting H. *Boundary-Layer Theory*. New York City: McGraw-Hill; 1979.
34. Lighthill MJ. On displacement thickness. *J Fluid Mech*. 1958;4(4):383-392. https://doi.org/10.1017/S0022112058000525
35. Van Rooij RPJOM. Modification of the boundary layer calculation in RFOIL for improved airfoil stall prediction. Report IW-96087R, the Netherlands, Delft University of Technology; 1996.
36. de Oliveira G, Pereira R, Timmer WA, van Rooij R. Improved airfoil polar predictions with data-driven boundary-layer closure relations. *J Phys: Conf Ser*. 2018;1037:022009. https://doi.org/10.1088/1742-6596/1037/2/022009
37. de Oliveira G, Pereira R, Ragni D, Kotsonis M. Modeling DBD plasma actuators in integral boundary layer formulation for application in panel methods. In: Proceedings of the 46th AIAA Plasmadynamics and Lasers Conference; 2015; Dallas, TX. https://doi.org/10.2514/6.2015-3367.
38. Bettermann D. Contribution a l'etude de la convection forcee turbulente le long de plaques rugueuses. *Int J Heat and Mass Transfer*. 1966;9(3):153-164. https://doi.org/10.1016/0017-9310(66)90014-7
39. Tani I. Some equilibrium turbulent boundary layers. *Fluid Dyn Res*. 1986;1(1):49-58. https://doi.org/10.1016/0169-5983(86)90006-7
40. Dunker S. Experiments in line vibration and associated drag for kites. In: Proceedings of the 23rd AIAA Aerodynamic Decelerator Systems Technology Conference; 2015; Daytona Beach, FL, USA:2154. https://doi.org/10.2514/6.2015-2154
41. Argatov I, Rautakorpi P, Silvennoinen R. Estimation of the mechanical energy output of the kite wind generator. *Renew Energy*. 2009;34(6):1525-1532. https://doi.org/10.1016/j.renene.2008.11.001
42. Kulfan BM. The CST universal parametric geometry representation method, recent extensions and applications. *Proc R Aeronaut Soc Conf*. 2007;114(1135):157-176. https://doi.org/10.1017/S0001924000003614
43. Ciampa PD, Zill T, Nagel B, et al. CST parametrization for unconventional aircraft design optimization. In: Proceedings of the 27th Congress of the International Council of the Aeronautical Sciences (ICAS), vol 11; 2010; Nice, France.
44. Straathof MH. Shape parameterization in aircraft design: a novel method, based on B-splines. *Ph.D. Thesis*; 2012. http://resolver.tudelft.nl/uuid:b4aee571-0489-42ff-ab55-d74e980f724a
45. Sripawadkul V, Padulo M, Guenov M. A comparison of airfoil shape parameterization techniques for early design optimization. In: Proceedings of the 13th AIAA/ISSMO Multidisciplinary Analysis Optimization Conference; 2010; Fort Worth, TX. https://doi.org/10.2514/6.2010-9050
46. Taylor RL, Oñate E, Ubach P-A. Finite element analysis of membrane structures. In: Oñate E, Kröplin B, eds. *Textile Composites and Inflatable Structures*, Computational Methods in Applied Sciences. Dordrecht: Springer Netherlands; 2005:47-68. https://doi.org/10.1007/1-4020-3317-6_4
47. Buhl T, Pedersen CBW, Sigmund O. Stiffness design of geometrically nonlinear structures using topology optimization. *Struct Multidisc Optim*. 2000;19(2):93-104. https://doi.org/10.1007/s001580050089
48. Koiter WT. On the principle of stationary complementary energy in the nonlinear theory of elasticity. *SIAM J Appl Math*. 1973;25(3):424-434. https://www.jstor.org/stable/2100113
49. Deb K, Pratap A, Agarwal S, Meyarivan TAMT. A fast and elitist multiobjective genetic algorithm: NSGA-II. *IEEE Trans Evol Comput*. 2002;6(2):182-197. https://doi.org/10.1109/4235.996017
50. de Rooij R, Abdalla MM. A finite element interior-point implementation of tension field theory. *Comput Struct*. 2015;151:30-41. https://doi.org/10.1016/j.compstruc.2015.01.007
51. Pipkin AC. Relaxed energy densities for large deformations of membranes. *IMA J Appl Math*. 1994;52(3):297-308. https://doi.org/10.1093/imamat/52.3.297

How to cite this article: Thedens P, de Oliveira G, Schmehl R. Ram-air kite airfoil and reinforcements optimization for airborne wind energy applications. *Wind Energy*. 2019;1–13. https://doi.org/10.1002/we.2313